Decoding Phases of Matter by Machine-Learning Raman Spectroscopy

Anyang Cui (崔安阳),[1] Kai Jiang (姜凯),[1] Minhong Jiang (江民红),[2] Liyan Shang (商丽燕),[1] Liangqing Zhu (朱亮清),[1] Zhigao Hu (胡志高),[1,3,4,*] Guisheng Xu (许桂生),[5] and Junhao Chu (褚君浩)[1,3,4]

[1] *Technical Center for Multifunctional Magneto-Optical Spectroscopy (Shanghai), Department of Materials, School of Physics and Electronic Science, East China Normal University, 200241 Shanghai, China*

[2] *Guangxi Key Laboratory of Information Materials, Department of Materials Science and Engineering, Guilin University of Electronic Technology, Guilin, 541004 Guangxi, China*

[3] *Collaborative Innovation Center of Extreme Optics, Shanxi University, Taiyuan, 030006 Shanxi, China*

[4] *Shanghai Institute of Intelligent Electronics & Systems, Fudan University, 200433 Shanghai, China*

[5] *Key Laboratory of Transparent Opto-Functional Advanced Inorganic Materials, Shanghai Institute of Ceramics, Chinese Academy of Sciences, 201899 Shanghai, China*

(Received 15 May 2019; revised manuscript received 26 September 2019; published 21 November 2019)

Phase transitions of condensed matter have long been a spotlight issue studied by extensive theoretical and experimental investigations. Machine learning can build an integral model-dominant workflow to statistically analyze the collective dynamics of materials and deduce the structure. We use a support-vector-machine algorithm to propose an effective method to recognize the orthorhombic, tetragonal, and cubic phases as well as to construct the phase diagram in ferroelectric crystals by mining and learning the behavioral vectors of the phonon vibrations in a crystalline lattice from Raman scattering, which is a tool typically used to detect structural properties at the molecular level. This study creates a unifying framework including material synthesis and characterization, feature engineering and principal-component analysis, learner evaluation and optimization, structure prediction, and future development of the model. It paves the way to the application of a generic approach for predicting unexplored structures and materials in the future.

DOI: 10.1103/PhysRevApplied.12.054049

I. INTRODUCTION

Machine learning, as a subfield of artificial intelligence and a powerful tool for the generation, testing, and refinement of scientific models for processing massive datasets, has gradually been applied in material science [1–5]. The success of materials informatics creates more opportunities for progress in material design, synthesis, experimental characterization, and computational modeling [6–13]. Of high interest is the use of machine learning to determine phases of matter [14–18]. Understanding structure and phase transition is an important topic in condensed-matter physics, and is generally dependent on the collective effects of structural, electronic, quantum, and topological dynamics. Traditional approaches to directly define a phase rely mainly on calculating order parameters, which may sometimes be confusing to physicists because some order parameters are unmeasurable, such as entanglement entropy, or cannot be identified, such as topologically ordered states [14,19,20]. Machine learning is helpful to resolve this undesirable situation. Neural-network models have been theoretically used to find the topological quantum phase transition [15,17], the many-body-localization transition in a disordered quantum spin chain [17], and the ferromagnetic-paramagnetic transition in the Ising model [14,16,17]. Furthermore, *k*-means clustering was used to determine the M_B-M_C phase diagram of $Pb(Mg_{1/3}Nb_{2/3})O_3$-$PbTiO_3$ crystals by the mining and learning of piezoelectric relaxation responses [18].

Typically, x-ray and neutron diffraction, magnetic and spin resonance, and molecular vibrational spectroscopy are useful and technically complementary for deducing structural information in multifield environments [21–24]. Exploring new material and structural properties is often assisted by methods such as computational simulation. Fortunately, the application of machine learning can build a unifying framework in material research, enabling the synergy of experimental characterization and analytic modeling [1]. For example, machine learning is capable of understanding spectral features from x-ray absorption spectra to interpret the structural and electronic properties of a material [9,25,26]. An appropriate machine learner

*zghu@ee.ecnu.edu.cn

and accumulative experimental dataset may result in a revolution to gradually transfer human-dominant study of material science to a machine-dominant one [3,7,8].

A highly correlated kernel model based on a Raman-scattering spectral database is developed here to recognize ferroelectric (F) phases and construct the phase diagram. Raman spectroscopy is used to provide a structural fingerprint at the molecular level, which is sensitive to nonuniform distortions of the crystal lattice in short-range ordering [27–31]. It provides crucial evidence toward demonstrating structural details of almost all known ferroelectrics, from Rochelle salt to $PbZr_xTi_{1-x}O_3$ and environment-friendly $(K,Na)NbO_3$ [32–39]. A large Raman spectral dataset can be built to develop predictive models for future structural investigations. We use a supervised support-vector-machine (SVM) algorithm to propose a kernel learner for deducing ferroelectric orthorhombic (O) and tetragonal (T) and paraelectric (P) cubic (C) phases. Finding the descriptors for a learner depends on quantifying thermal-phonon dynamics from a scattering spectral dataset. The optimized model learns the rules that underlie Raman spectra by assessing phonon behaviors of lattice vibrations. The present study demonstrates an integral process in machine learning ferroelectric phases: sample preparation and experimental characterization; data generation and engineering; model selection, evaluation, and optimization; structural prediction.

II. MATERIALS AND METHODS

The $0.95K_{0.5}Na_{0.5}NbO_3$-$0.05LiNbO_3$ (KNN1) single crystal is grown by the flux-Bridgman method. The 0.25 at. % Mn-doped $99.6K_{0.5}Na_{0.5}NbO_3$-$0.4LiBiO_3$ (KNN2), 0.37 at. % Mn-doped $99.6K_{0.5}Na_{0.5}NbO_3$-$0.4LiBiO_3$ (KNN3), and 0.6 at. % Cu-doped $99.6K_{0.5}Na_{0.5}NbO_3$-$0.4LiBiO_3$ (KNN4) single crystals are prepared by the seed-free solid-state crystal-growth method. The synthesis procedures can be found elsewhere [32,33,40–44]. Raman spectra are recorded with use of a Jobin-Yvon LabRAM HR Evolution spectrometer and a THMSE 600 heating and cooling stage (Linkam Scientific Instruments) in the thermal cycle. A ×50 microscope with a working distance of 18 mm and an excitation laser with a wavelength of 532 nm are used. The spectral resolution is less than 1 cm^{-1}. The laser power focused on the sample is about 4 mW, so the heating effect from the laser beam can be ignored. Raman signals are collected by an air-cooled charge-coupled device with a grating with 1800 grooves/mm. For comparison and for removal of the contribution from the Bose-Einstein population factor, Raman data are corrected by the Bose-Einstein temperature factor, $n(\omega,T) = 1/[\exp(\hbar\omega/kT) - 1]$, where $\hbar$, ω, k, and T are the reduced Planck constant, phonon wave number, Boltzmann constant, and temperature, respectively. Descriptor generation depends on quantifying phonon dynamics by decomposing Raman scattering peaks into a series of bands with the assumption of a Lorentzian-line-shape approximation according to the damped-harmonic-oscillator model. Because the specific descriptor matrix $\mathbf{x}_{ij}$ is composed of scattering characteristics and a derived parameter, intensity $I(\omega)$, phonon frequency ω, linewidth W, and $I(\omega)/W$ with different dimensions and units, the input matrix is scaled and normalized to ensure comparability among descriptor vectors and improve the performance of the classifier. All data analysis and visualization is supported and processed by an open-source program and PYTHON packages, scikit-learn and matplotlib [45,46].

III. RESULTS AND DISCUSSION

Machine learning Raman spectra based on the radial-basis-function- (RBF) kernel SVM algorithm is used to realize a binary classifier for identifying F and P phases, and also a three-classification learner for O, T, and C phases. Figure 1 shows the fundamental framework for learning phase recognition. Depending on the infinite-dimensional mapping mechanism by the Gaussian kernel, the model is expected to learn hundreds of Raman spectra. We first create an experimental dataset by characterizing Raman scattering from 356 spectra in total at 150–800 K of doped $K_{0.5}Na_{0.5}NbO_3$ (KNN) single crystals (KNN1, KNN2, KNN3, and KNN4) prepared by different synthesis methods. Each input vector is associated with an original spectrum at the related temperature and phase label.

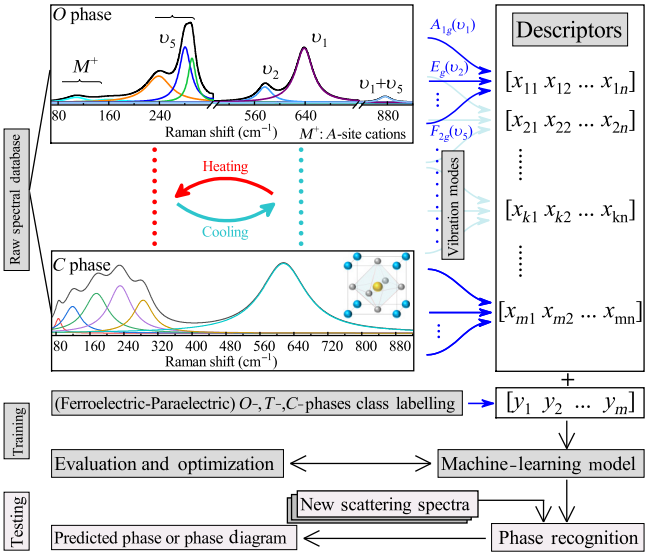

FIG. 1. Workflow of the machine-learning Raman-spectrum-based ferroelectric-phase-identification framework using a supervised algorithm, which contains descriptor generation, training, and testing procedures. Solid blue arrows show that descriptors $\mathbf{x}_{ij}$ collect information on each phonon [$A_{1g}(\nu_1)$, $E_g(\nu_2)$, M^+, etc. marked in the spectral examples] dynamics from the fitted scattering peaks under a thermal process.

All input vectors collected from the experimental dataset are randomly divided into a test set and a training set in a ratio of 0.2:0.8, where the supervised SVM algorithm allows the assignment of an objective label to follow the corresponding individual input vector. Simultaneously, a trained model can predict each test vector one by one, and mark the predicted class with the known temperature. In addition, a k-fold cross-validator is used to evaluate the performance of the trained model by providing training and cross-validation indices to split the dataset into k consecutive folds, where an appropriate and common $k = 10$ is set in this study. During the tenfold cross-validation, each fold is used once as a validation set, while the nine remaining folds form the training set.

The core issue dominating reliable prediction is to understand the physical connection between the set of descriptive parameters (descriptors) and the phase-transition mechanism. In other words, feature engineering requires insight into the underlying physical nature of the raw spectra. Ghiringhelli *et al.* [6] proposed the discrete dataset $\{P_k, \mathbf{x}_{ij}\}$ to define the physical relationship between the descriptor vector $\mathbf{x}_{ij}$ and the material property P_k, which is associated with the phase-transition property in this study. Generally, the phase-transition property P_k can be characterized by a string of structural variables, such as spontaneous polarization P_S, molecule polarizability α_{ij}, bonding strength, bond length, and bond-angle distortion $\Delta\vartheta$, as $P_k\{P_S, \alpha_{ij}, \Delta\vartheta \ldots\}$. Then, the generation of the descriptor vector $\mathbf{x}_{ij}$ depends on linking the physical correlation with $P_k\{P_S, \alpha_{ij}, \Delta\vartheta \ldots\}$.

Studying the phase transition by Raman scattering focuses on exploring the phonon characteristics of each vibrational mode [27–30]. The deconvolutions of the Raman spectra present quantitative information (peak position, linewidth, and intensity) on each scattering peak by using a series of Lorentzian curve fittings. For example, as shown in Fig. 1, two spectra observed at 153 and 693 K are associated with the O phase and the C phase, respectively, showing the fitted peaks corresponding to various phonon modes. We construct the set of descriptors associated with thermal-phonon dynamics of the ferroelectric KNN lattice. The RBF SVM model learns the phonon characteristics and interprets their variations for different temperatures and phases. In detail, the KNN lattice has the space group $Amm2$ (C_{2v}^{14}) with Raman-active $4A_1 + 4B_1 + 3B_2 + A_2$ optical modes. Except for the $B_1 + B_2 + A_1$ mode at around 860 cm^{-1}, which is a longitudinal optical vibration mode, the other modes are transverse optical vibration modes. The molecular vibrations of the doped KNN lattice consist of the translational modes of the A-site alkaline cation (M^+) and internal modes of octahedral NbO_6, the $1A_{1g}(\nu_1) + 1E_g(\nu_2) + 2F_{1u}(\nu_3, \nu_4) + 1F_{2g}(\nu_5) + 1F_{2u}(\nu_6)$ stretching and bending modes. As plotted in Fig. 1, the Raman spectra show that the phonon of each vibration is mainly excited below 300 cm^{-1}, at 500–650 cm^{-1}, and near 860 cm^{-1}. With the wave number increasing from 80 to 900 cm^{-1}, in turn, the colored Lorentzian-shaped peaks reflect the lattice vibrational modes of M^+, ν_5, ν_2, ν_1, and $\nu_1 + \nu_5$, respectively. The $\nu_1 + \nu_5$ mode in the C phase disappears. Temperature dependence of the phonon frequency ω is regarded as one of the criteria to study phase transitions. However, the phonon frequency is sensitive to the change of the covalent-bond length. The frequency shift is additionally derived from thermally induced distortion of the lattice and phonon-phonon interaction. Descriptors involving frequency-related items would enable the classifier to distinguish a phase transition (atom arrangement) from the other factors from the anharmonicity of the potential acting on atoms in the lattice. To ensure the classification output derives from the phase transition and not from factors mentioned above, the optimized relaxation factor C of the supervised RBF SVM algorithm is generally used to increase the accuracy and robustness of the classifier by examining the error samples and trading off the input against maximization of the decision function's margin.

Thermally induced phase transition of the ferroelectric KNN crystal is associated with the discontinuous evolution of the molecular polarizability α_{ij}. As a function of the coordinate Q_k displacement of nuclei ($\partial\alpha_{ij}/\partial Q_k$), the polarizability represents the dynamical interaction in a bound system with the external field of light, and reflects the molecular symmetry. If one solely considers the anti-Stokes line, the Raman-scattering intensity is proportional to $(\partial\alpha_{ij}/\partial Q_k)_0^2$, where $()_0$ denotes the value for a molecule in the equilibrium state [27,47]. The set of descriptors $\mathbf{x}_{ij}$ additionally consists of the scattering characteristics related to intensity $I(\omega)$ and linewidth W, where the latter is typically used to study the degree of crystallinity experimentally. A physical representation of the scattering frequency, intensity, and linewidth can be defined with respect to the Gaussian-distribution eigenfunction as

$$I(\omega) \propto \int e^{[-(qL/2)^2]} \frac{d\mathbf{q}^2}{[\omega - \omega(\mathbf{q})^2] + \left(\frac{W_0}{2}\right)^2}, \qquad (1)$$

where $\mathbf{q}$ is the wave vector, L is the equivalent diameter of a molecule, and W_0 is the sum of the peak linewidth of the bulk crystal and the spectrometer broadening [48]. The linewidth of the scattering peak for the transverse optical mode is proportional to the bond-angle distortion $\Delta\vartheta$ of the molecule. The equivalent diameter L in a symmetric crystallite reflects the defect concentration of the crystal. With increase of temperature, phase transition is accompanied by thermal evolution of these lattice parameters. An appropriate derived parameter, $I(\omega)/W$, based on the linewidth and intensity is also chosen as a component of the input descriptors, because the derived parameter will increase the robustness and accuracy of the model

during the feature engineering. Consequently, the multidimensional descriptor vector $\mathbf{x}_{ij}$ from phonon dynamics over a range of temperatures as $\mathbf{x}_{ij} : \{\omega, I(\omega), W, I(\omega)/W\}$ is a physically meaningful parameter to describe ferroelectric phase transition. In detail, a descriptor vector consists of four components, where the first component is the phonon frequency, the second and third components are the corresponding intensity and linewidth, and the fourth component is the derived parameter $I(\omega)/W$. All components are extracted from Raman spectroscopy at the frequency of 80 to 900 cm^{-1}.

Each set of descriptors could correspond to O, T, and C phases or F and P phases, which are labeled as the objective variables y_i of integers 0, 1, or 2, respectively. Whole descriptors $\mathbf{x}_{ij}$ and the label vector y_i with the optimized hyperparameters are input synchronously and used to build the classifier. However, during the setting up of the descriptor and objective matrices, we notice to solve the individual difference problem for each sample with the different number of features for various phases and temperatures. To increase the model performance and ensure learning of all the phonon characteristics collected at each corresponding temperature, the model requires the vector space contain all phonon characteristics collected from the Raman spectrum with the greatest number of phonon modes. Each phonon characteristic is considered as a part of the vector space. For other spectra, if their number of phonon modes is less than the space capacity, the program adds a null bit into this vector space. In this case, the model can be trained by learning all phonon information extracted from the original spectrum.

The supervised RBF SVM algorithm requires the input descriptors in the input space Π to be implicitly mapped into an infinite-dimensional feature space Γ, $\Phi : \Pi \rightarrow \Gamma$, by a Gaussian kernel, $K(x^i, x^j) = \Phi(x^i)^T\Phi(x^j) = \exp[-(\| x^i - x^j \|^2/2\sigma^2)]$, where the corresponding conversion function is $\Phi(x) = \sum_{i=0}^{\infty} \exp(-x^2)\sqrt{(2^i/i!)}x^i$, x^i and x^j are the input samples, and σ is the standard deviation. This kernel function is a monotonic function of $\| x^i - x^j \|^2$, which is the Euclidean distance between vectors $\mathbf{x}^i$ and $\mathbf{x}^j$. Then a set of hyperplanes, constructed in the space Γ, realize the maximum margin to support vectors (the nearest training data point) of any class. There are two key parameters for optimizing the RBF SVM model, C and γ. The relaxation factor C trades off the correct classification of the training data against maximization of the decision function's margin. The parameter γ intuitively defines how far the influence of a single training sample reaches, satisfying $\gamma = 1/(2\sigma^2)$. The evaluation and optimization of the model is an indispensable process before the prediction of a new spectrum. The different values of C and γ directly determine the bias and variance of the RBF SVM learner, which represent the error from a false assumption and the training set's small fluctuations, respectively. We use a k-fold cross-validation method to evaluate the model by calculating the cross-validation accuracy for different values of C and γ as well as to study the learning curve, which is used to estimate the performance (overfitting or underfitting) of the trained model. The cross-validation accuracy for different values of C and γ can be examined from a parameter heatmap. The learning curve and parameter heatmap used as the evaluation tools for model performance are not restricted by the size of the training dataset.

Figure 2(a) shows a numerical heatmap of the cross-validation accuracy as a function of C and γ for F-P classification. The greatest validation score is 0.997, for $\gamma = 0.1$ and $C = 10$ and for $\gamma = 0.01$ and $C = 100$. For the O-T-C phase transition, the greatest cross-validation accuracy is 0.987, for $\gamma = 0.1$ and $C = 10$ and for $\gamma = 0.1$ and $C = 1000$ [see Fig. 2(b)]. The learning curves [Fig. 2(c)] confirm the excellent validation performance of the model without underfitting or overfitting. The cross-validation accuracy increases gradually, approaching the training performance of more than 0.99. Detailed cross-validation results are presented in Fig. S1in Supplemental Material [49].

The well-trained classifier predicts the phase diagram of two sets of new Raman spectra of KNN crystals prepared by different methods. The temperature-dependent phase diagram in Fig. 2(d) is predicted and reveals that the Curie temperature (T_C) is at around 688 K, corresponding to P-F or C-T transition, and the T-O phase transition occurs near 413 K. Next we investigate details of the test dataset of scattering spectra (163—768 K) in Fig. 2(e) to check the prediction accuracy. Phonon modes of $A_{1g}(\nu_1)$ (600 cm^{-1}) and $F_{2g}(\nu_5)$ (260 cm^{-1}) as strong scattering are associated with a near-perfect equilateral octahedral symmetry believed to be C_{2v}^{14}. As the temperature rises from 163 to 413 K and from 418 to 688 K, the apparent redshift of the peaks near 270 and 600 cm^{-1} results from phonon-phonon interaction and thermally induced deformation of the lattice. In terms of the first-order phase transition of the KNN lattice, the temperature (T) is considered as the only variable of the system to investigate the transition process. Thermal dynamic equilibrium can ensure the Gibbs free energy [$G(T)$] is minimized at the phase transition. The change of entropy and spontaneous polarization, $-\partial G/\partial T$, is intrinsically discontinuous at the T-O or C-T transition. Symmetry breaking and structural reconstruction in lattices are directly related to transformation of internal vibrational modes. Thus, the phonon frequencies ν_1 and ν_5 will shift during the phase transition. The shifts marked by asterisks at 413–418 K correspond to the T-O transition. At high temperature, corresponding to higher lattice symmetry, the peaks gradually become wider than those at low temperatures. The $\nu_1 + \nu_5$ peak near 860 cm^{-1} almost disappears in the C phase. A high-symmetry C phase is associated with temperatures above 688 K. Therefore, on the basis of the comparison between the spectral

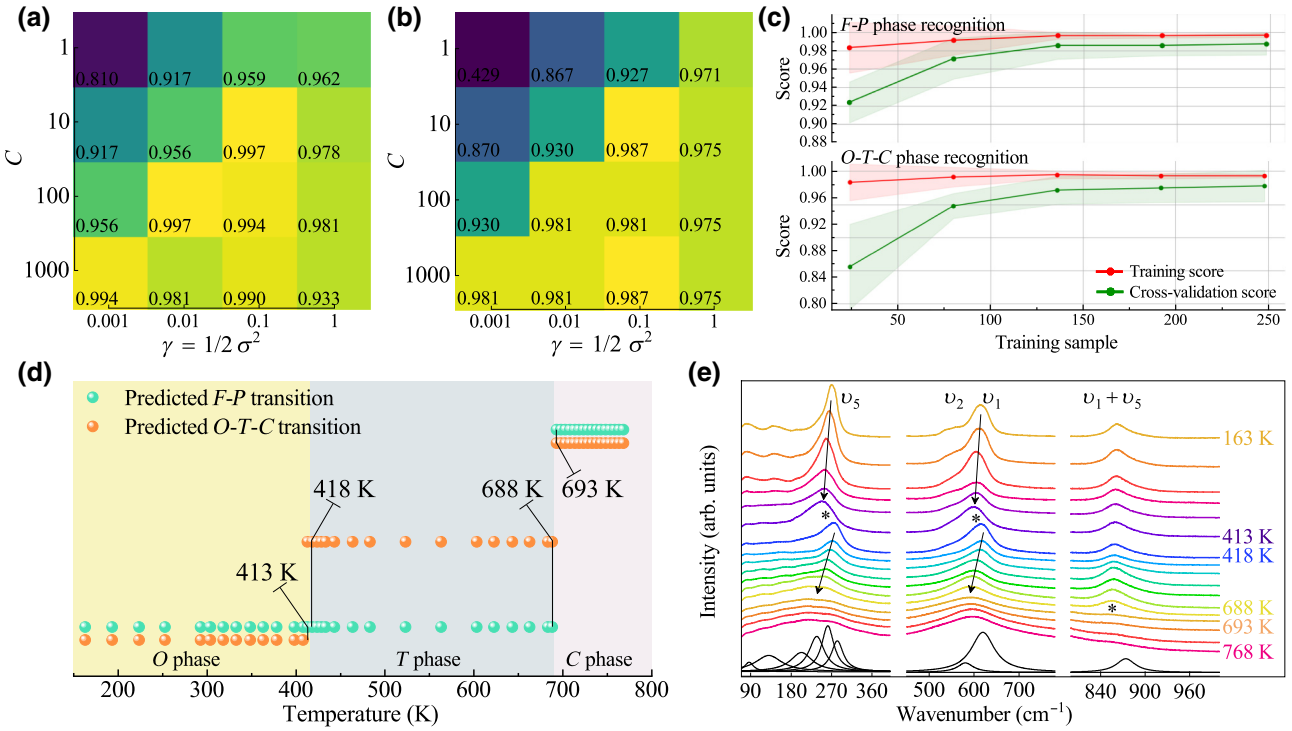

FIG. 2. Numerical heatmap of the cross-validation accuracy of the model as a function of C and γ for (a) F-P and (b) O-T-C phase transitions, respectively. (c) Learning curves of models for $\gamma = 0.1$ and $C = 10$. The number of training samples is 249, accounting for 80% of the training dataset, while the remaining 20% is used for random cross-validation. (d) Predicted temperature-dependent phase diagram. O-T and T-C (F-P) phase transitions are predicted to occur at around 413 and 688 K (T_C), respectively. (e) Raman spectra as the test dataset collected in the temperature range from 163 to 768 K. Lorentzian-shaped deconvolution at 413 K distinguishes the different phonons. The arrows mark thermally induced redshift. The asterisks mark the change of peaks at the phase transition.

analysis and the predicted results, the RBF SVM model exhibits appropriate performance in predicting the phase and constructing a predicted temperature-dependent phase diagram from test spectra.

Another set of test data come from the literature [32,40], to avoid the effect of similar doping compositions of other KNN samples. The classifier is retrained with the greatest validation score of more than 0.99, as shown in Figs. S2(a)–S2(d)in Supplemental Material [49]. In this case, the predicted phase diagram [Fig. S2(e) in Supplemental Material] shows that the O-T phase transition is located at 420–440 K, and the F-P (T-C) transition temperature (T_C) is at 700–710 K. This result is consistent with the result reported according to temperature-dependent dielectric permittivity [40].

Data heterogeneity of the Raman spectral database for one material is derived from the structural properties themselves, such as phase transition, doping, lattice polarization, crystallinity, and anisotropy, or some external factors, such as temperature, pressure, electric field, or magnetic field. A robust classifier should increase precision and generalization ability for phase recognition from temperature-dependent Raman spectra by enriching the experimental training dataset, except for the appropriate collection of the descriptor. However, with the available data increasing, this machine learner would experience new challenges, such as curse of dimensionality and more noise. The curse of dimensionality is a big drawback for the RBF SVM model with the data expansion, resulting in decreased computational capacity and an unexpected prediction. Fortunately, principal-component analysis (PCA) as an unsupervised algorithm can effectively overcome the problems and realize data denoising and dimensionality reduction for an expanded Raman spectral database [18].

The PCA procedure allows the input matrix X involving temperature-dependent phonon behavior to be preprocessed before the eigenvalues and eigenvectors are solved using singular-value decomposition. All columns in eigenvector matrix P are sorted in order of decreasing eigenvalue. Then the expected matrix Y $(m \times n)$ is obtained according to $Y^T = PX^T$, where m is the sample size, n is the number of features, and each column of Y is the linearly uncorrelated principal component partially interpreting phonon information from the raw Raman spectra. The explained variance ratio (EVR, η) is the percentage of variance explained by the selected first k principal components to the total variance of whole dataset, as given by $\eta = 1 - \sum_k x_{ii} / \sum_n x_{ii}$. In Fig. 3(a), we examine the EVR of all

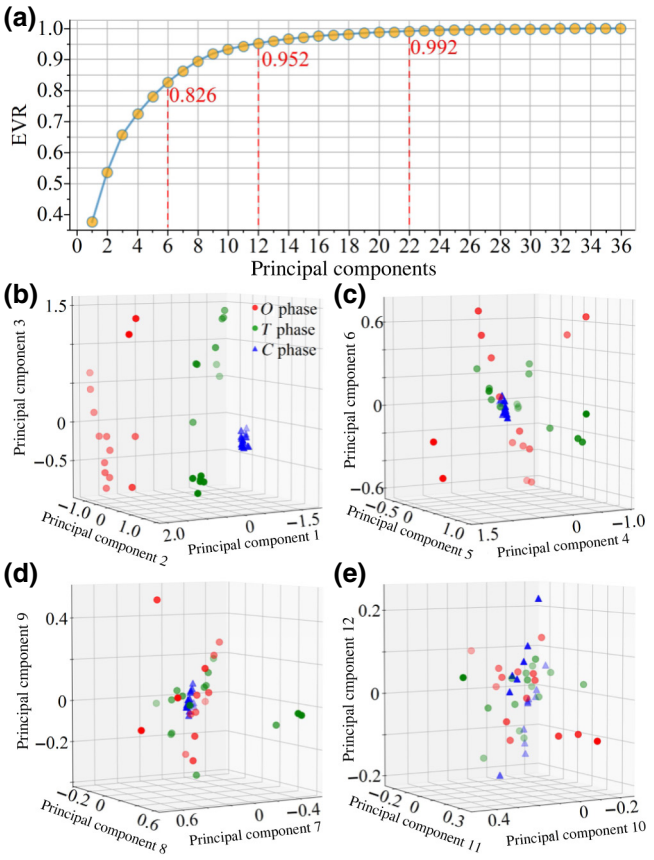

FIG. 3. (a) Ratio of the cumulative variance explained by the principal components. (b)–(e) The relative distribution of the first 12 principal components.

principal components representing a random selection of a raw spectral dataset, which is extracted from O, T, and C phases. The first six components can explain 82.6% of the variance. It will require the first 12 and 22 components for the EVR to reach more than 95% or 99%, respectively. We define a three-dimensional space to visualize the relative distribution of the first 12 components in Figs. 3(b)–3(e). As the known-phase data, the individual sample (each row of Y) with its phase label (O, T, and C) is depicted by different markers. The first six components, especially the first three as the most-principal components, can clearly separate the data samples into O, T, and C phases according to their top-three EVRs. Compared with the data representing the O phase or T phase, the data for the C phase exhibit less dispersion and variance. With the decline in the importance of the component, the data for the O and T phases gradually converge to those for the C phase, leading to an ambiguous distribution. Therefore, PCA technology efficiently reduces the dimensionality of raw spectra by extracting the eigenvalues, whose corresponding eigenvectors can maintain phonon characteristics among different phases. The use of the unsupervised method further results in the phase-recognition model better understanding the variation of the phase transition with the basic phonon information. It is beneficial to not only increase the performance and accuracy of a ferroelectric phase classifier but also to increase the efficiency and robustness.

The use of PCA and a classifier algorithm provides an additional opportunity to process a larger dataset based on thousands of Raman spectra. In addition to PCA, RBF SVM, and algorithms such as neural networks, other algorithms or an ensemble of different algorithms could also be used to build a structure classifier [16,18]. Data on molecular vibration and phonon dynamics in a broader range of materials beyond ferroelectrics are easily collected from Raman-scattering or infrared-reflection techniques. Their structural recognition learners would expect to be efficiently established on the basis of a database of molecular spectra by learning the lattice details of the collected phonon vibration dynamics. Besides, a more-robust integrated learner for phase identification may further require continuous improvement of the programmable framework. An additional way to improve a good phase-prediction learner is to design it to obtain the probabilities of each phase instead of a single class. The appropriate probability results of structural phase investigations would provide more insights for understanding the structural information of materials in condensed-matter systems. This study provides a road map and effective attempts at structural phase recognition by machine learning Raman scattering. Future studies are expected to realize a powerful machine-oriented model for determining phases and more structural properties of materials.

IV. CONCLUSION

In summary, a well-trained machine-learning model based on Raman spectra is capable of determining ferroelectric phases by mining phonon dynamics. This work provides a clear demonstration of the integral workflow for building a phase classifier from material synthesis to structural prediction. It highlights that model evaluation and a flexible optimization process can clearly ensure the trained model is the best optimized one. The present method could be extended to broader applications on organic or inorganic materials, chemical representations, and biological recognition [50,51].

ACKNOWLEDGMENTS

This work was financially supported by the National Natural Science Foundation of China (Grants No. 91833303 and No. 61674057), the National Key R&D Program of China (Grants No. 2017YFA0303403 and No. 2018YFB0406500), the Projects of the Science and Technology Commission of Shanghai Municipality (Grants No, 18JC1412400, No. 18YF1407200, No. 18YF1407000, and

No. 19511120100), and the Program for Professor of Special Appointment (Eastern Scholar) at Shanghai Institutions of Higher Learning. We thank Dr. Yan Ye and Dr. Liping Xu for data support.

[1] K. T. Butler, D. W. Davies, H. Cartwright, O. Isayev, and A. Walsh, Machine learning for molecular and materials science, Nature **559**, 547 (2018).

[2] S. V. Kalinin, B. G. Sumpter, and R. K. Archibald, Big-deep-smart data in imaging for guiding materials design, Nat. Mater. **14**, 973 (2015).

[3] W. Ye, C. Chen, S. Dwaraknath, A. Jain, S. P. Ong, and K. A. Persson, Harnessing the materials project for machine-learning and accelerated discovery, MRS Bull. **43**, 664 (2018).

[4] J. P. Correa-Baena, K. Hippalgaonkar, J. van Duren, S. Jaffer, V. R. Chandrasekhar, V. Stevanovic, C. Wadia, S. Guha, and T. Buonassisi, Accelerating materials development via automation, machine learning, and high-performance computing, Joule **2**, 1410 (2018).

[5] Y. Liu, T. Zhao, W. Ju, and S. Shi, Materials discovery and design using machine learning, J. Materiomics **3**, 159 (2017).

[6] L. M. Ghiringhelli, J. Vybiral, S. V. Levchenko, C. Draxl, and M. Scheffler, Big Data of Materials Science: Critical Role of the Descriptor, Phys. Rev. Lett. **114**, 105503 (2015).

[7] K. Takahashi and Y. Tanaka, Materials informatics: A journey towards material design and synthesis, Dalton Trans. **45**, 10497 (2016).

[8] M. L. Green, C. L. Choi, J. R. Hattrick-Simpers, A. M. Joshi, I. Takeuchi, S. C. Barron, E. Campo, T. Chiang, S. Empedocles, J. M. Gregoire, A. G. Kusne, J. Martin, A. Mehta, K. Persson, Z. Trautt, J. Van Duren, and A. Zakutayev, Fulfilling the promise of the materials genome initiative with high-throughput experimental methodologies, Appl. Phys. Rev. **4**, 011105 (2017).

[9] M. R. Carbone, S. Yoo, M. Topsakal, and D. Lu, Classification of local chemical environments from x-ray absorption spectra using supervised machine learning, Phys. Rev. Mater. **3**, 033604 (2019).

[10] C. Nyshadham, M. Rupp, B. Bekker, A. V. Shapeev, T. Mueller, C. W. Rosenbrock, G. Csányi, D. W. Wingate, and G. L. W. Hart, Machine-learned multi-system surrogate models for materials prediction, npj Comput. Mater. **5**, 51 (2019).

[11] K. Ghosh, A. Stuke, M. Todorović, P. B. Jørgensen, M. N. Schmidt, A. Vehtari, and P. Rinke, Deep learning spectroscopy: Neural networks for molecular excitation spectra, Adv. Sci. **6**, 1801367 (2019).

[12] M. Umehara, H. S. Stein, D. Guevarra, P. F. Newhouse, D. A. Boyd, and J. M. Gregoire, Analyzing machine learning models to accelerate generation of fundamental materials insights, npj Comput. Mater. **5**, 34 (2019).

[13] E. Kim, K. Huang, A. Saunders, A. McCallum, G. Ceder, and E. Olivetti, Materials synthesis insights from scientific literature via text extraction and machine learning, Chem. Mater. **29**, 9436 (2017).

[14] A. Tanaka and A. Tomiya, Detection of phase transition via convolutional neural networks, J. Phys. Soc. Jpn. **86**, 063001 (2017).

[15] Y. Zhang and E. A. Kim, Quantum Loop Topography for Machine Learning, Phys. Rev. Lett. **118**, 216401 (2017).

[16] J. Carrasquilla and R. G. Melko, Machine learning phases of matter, Nat. Phys. **13**, 431 (2017).

[17] E. P. L. van Nieuwenburg, Y. H. Liu, and S. D. Huber, Learning phase transitions by confusion, Nat. Phys. **13**, 435 (2017).

[18] L. Li, Y. Yang, D. Zhang, Z. G. Ye, S. Jesse, S. V. Kalinin, and R. K. Vasudevan, Machine learning-enabled identification of material phase transitions based on experimental data: Exploring collective dynamics in ferroelectric relaxors, Sci. Adv. **4**, eaap8672 (2018).

[19] X. G. Wen, Topological orders in rigid states, Int. J. Mod. Phys. B **4**, 239 (1990).

[20] A. Kitaev and J. Preskill, Topological Entanglement Entropy, Phys. Rev. Lett. **96**, 110404 (2006).

[21] J. Yan, Y. Zhang, P. Kim, and A. Pinczuk, Electric Field Effect Tuning of Electron-Phonon Coupling in Graphene, Phys. Rev. Lett. **98**, 166802 (2007).

[22] C. Ferrante, A. Virga, L. Benfatto, M. Martinati, D. De Fazio, U. Sassi, C. Fasolato, A. K. Ott, P. Postorino, D. Yoon, G. Cerullo, F. Mauri, A. C. Ferrari, and T. Scopigno, Raman spectroscopy of graphene under ultrafast laser excitation, Nat. Commun. **9**, 308 (2018).

[23] Z. H. Duan, P. Chang, Z. G. Hu, J. X. Wang, G. S. Wang, X. L. Dong, and J. H. Chu, Temperature dependent Raman scattering and far-infrared reflectance spectra of MgO modified $Pb_{0.99}(Zr_{0.95}Ti_{0.05})_{0.98}Nb_{0.02}O_3$ ceramics: A composition effect, J. Appl. Phys. **116**, 093513 (2014).

[24] M. Kim, X. M. Chen, Y. I. Joe, E. Fradkin, P. Abbamonte, and S. L. Cooper, Mapping the Magnetostructural Quantum Phases of Mn_3O_4, Phys. Rev. Lett. **104**, 136402 (2010).

[25] C. Zheng, K. Mathew, C. Chen, Y. Chen, H. Tang, A. Dozier, J. J. Kas, F. D. Vila, J. J. Rehr, L. F. J. Piper, K. A. Persson, S. P. Ong, Author correction: Automated generation and ensemble-learned matching of x-ray absorption spectra, npj Comput. Mater. **4**, 12 (2018).

[26] J. Timoshenko, D. Lu, Y. Lin, and A. I. Frenkel, Supervised machine-learning-based determination of three-dimensional structure of metallic nanoparticles, J. Phys. Chem. Lett. **8**, 5091 (2017).

[27] A. Cui, Y. Ye, L. Zheng, K. Jiang, L. Zhu, L. Shang, Y. Li, Z. Hu, and J. Chu, Exploring lattice symmetry evolution with discontinuous phase transition by Raman scattering criteria: The single-crystalline $(K, Na)NbO_3$ model system, Phys. Rev. B **100**, 024102 (2019).

[28] K. Kakimoto, K. Akao, Y. P. Guo, and H. Ohsato, Raman scattering study of piezoelectric $(Na_{0.5}K_{0.5})NbO_3$-$LiNbO_3$ ceramics, Jpn. J. Appl. Phys. **44**, 7064 (2005).

[29] N. Klein, E. Hollenstein, D. Damjanovic, H. J. Trodahl, N. Setter, and M. Kuball, A study of the phase diagram of $(K, Na, Li)NbO_3$ determined by dielectric and piezoelectric measurements, and Raman spectroscopy, J. Appl. Phys. **102**, 014112 (2007).

[30] H. J. Trodahl, N. Klein, D. Damjanovic, N. Setter, B. Ludbrook, D. Rytz, and M. Kuball, Raman spectroscopy of $(K, Na)NbO_3$ and $(K, Na)_{1-x}Li_xNbO_3$, Appl. Phys. Lett. **93**, 262901 (2008).

[31] K. Jiang, L. P. Xu, J. Z. Zhang, Z. G. Hu, and J. H. Chu, in *Structural Transformations in Ferroelectrics Discovered by Raman Spectroscopy, Raman Spectroscopy*, edited by Gustavo M. do Nascimento (INTECH Open Access Publishers, Vienna, 2018), Chap. 12.

[32] L. P. Xu, K. Jiang, J. Z. Zhang, G. S. Xu, Z. G. Hu, and J. H. Chu, Phase transitions and thermotropic phase boundaries in MnO_2-doped $(K_{0.5}Na_{0.5})NbO_3$-$0.05LiNbO_3$ single crystals: Raman scattering evidence at elevated temperatures, Appl. Phys. Lett. **106**, 122901 (2015).

[33] A. Y. Cui, K. Jiang, P. Zhang, L. P. Xu, G. S. Xu, X. M. Chen, Z. G. Hu, and J. H. Chu, In situ exploration of thermal-induced domain evolution with phase transition in $LiNbO_3$-modified $K_{0.5}Na_{0.5}NbO_3$ single crystal, J. Phys. Chem. C **121**, 14322 (2017).

[34] T. M. K. Nedungadi, Raman effect in Rochelle salt crystals, Indian Acad. Sci. **11**, 413 (1940).

[35] V. Winterfeldt, Raman spectroscopic investigation of ferroelectric phase transitions in Rochelle salt, Phys. Status Sol. (b) **100**, 235 (1980).

[36] Y. Saito, H. Takao, T. Tani, T. Nonoyama, K. Takatori, T. Homma, T. Nagaya, and M. Nakamura, Lead-free piezoceramics, Nature **432**, 84 (2004).

[37] E. Cross, Lead-free at last, Nature **432**, 24 (2004).

[38] K. Xu, J. Li, X. Lv, J. Wu, X. Zhang, D. Xiao, and J. Zhu, Superior piezoelectric properties in potassium-sodium niobate lead-free ceramics, Adv. Mater. **28**, 8519 (2016).

[39] X. P. Wang, J. G. Wu, D. Q. Xiao, J. G. Zhu, X. J. Cheng, T. Zheng, B. Y. Zhang, X. J. Lou, and X. J. Wang, Giant piezoelectricity in potassium-sodium niobate lead-free ceramics, J. Am. Chem. Soc. **136**, 2905 (2014).

[40] Y. Liu, G. Xu, J. Liu, D. Yang, and X. Chen, Dielectric, piezoelectric properties of MnO_2-doped $(K_{0.5}Na_{0.5})NbO_3$-$0.05LiNbO_3$ crystal grown by Flux-Bridgman method, J. Alloys Compd. **603**, 95 (2014).

[41] M. H. Jiang, C. A. Randall, H. Z. Guo, G. H. Rao, R. Tu, Z. F. Gu, G. Cheng, X. Y. Liu, J. W. Zhang, and Y. X. Li, Seed-free solid-state growth of large lead-free piezoelectric single crystals: $(Na_{1/2}K_{1/2})NbO_3$, J. Am. Ceram. Soc. **98**, 2988 (2015).

[42] J. G. Song, C. Y. Hao, Y. F. Yan, J. W. Zhang, L. Li, and M. H. Jiang, Enhanced piezoelectric property and microstructure of large $CaZrO_3$-doped $Na_{0.5}K_{0.5}NbO_3$-based single crystal with 20 mm over, Mater. Lett. **204**, 19 (2017).

[43] M. H. Jiang, S. N. Han, J. W. Zhang, J. G. Song, C. Y. Hao, M. J. Deng, L. J. Ge, Z. F. Gu, and X. Y. Liu, Large-scale grain growth in the solid-state process: From "abnormal" to "normal", J. Cryst. Growth **483**, 258 (2018).

[44] C. Y. Hao, Z. F. Gu, G. Cheng, L. Li, J. W. Zhang, J. G. Song, Y. F. Yan, and M. H. Jiang, Composition design and electrical property of a pure $K_xNa_{1-x}NbO_3$ single crystal fabricated by the seed-free solid-state crystal growth, J. Mater. Sci. - Mater. Electron. **28**, 18357 (2017).

[45] F. Pedregosa, G. Varoquaux, A. Gramfort, V. Michel, B. Thirion, O. Grisel, M. Blondel, P. Prettenhofer, R. Weiss, V. Dubourg, J. Vanderplas, A. Passos, D. Cournapeau, M. Brucher, M. Perrot, and É. Duchesnay, Scikit-learn: Machine learning in Python, J. Mach. Learn. Res. **12**, 2825 (2011).

[46] J. D. Hunter, Matplotlib: A 2D graphics environment, Comput. Sci. Eng. **9**, 90 (2007).

[47] D. A. Long, *Raman Spectroscopy* (McGraw-Hill International Book Company, New York, 1977).

[48] H. Richter, Z. P. Wang, and L. Ley, The one phonon Raman spectrum in microcrystalline silicon, Solid State Commun. **39**, 625 (1981).

[49] See Supplemental Material at http://link.aps.org/supplemental/10.1103/PhysRevApplied.12.054049 for additional simulations and results.

[50] R. Gómez-Bombarelli *et al.*, Design of effcient molecular organic light-emitting diodes by a high-throughput virtual screening and experimental approach, Nat. Mater. **15**, 1120 (2016).

[51] M. Bjornmalm, M. Faria, and F. Caruso, Increasing the impact of materials in and beyond bio-nano science, J. Am. Chem. Soc. **138**, 13449 (2016).